Measuring the [C II]-to-H I connection in high-redshift absorption-selected galaxies

Gaurav Senthil Kumar

Lund Observatory
Lund University

2022-EXA199

Degree project of 15 higher education credits

Supervisors:
Kasper Elm Heintz, University of Copenhagen
Oscar Agertz, Lund University

Lund Observatory
Box 43
SE-221 00 Lund
Sweden

Abstract

H I neutral gas is the basic building block of galaxies. It dictates the star formation rate and hence the metal enrichment rates within high redshift galaxies. H I neutral gas cannot be directly observed beyond $z \approx 0.38$ due to the weakness of the 21 cm transition, therefore alternate methods need to be developed for studying high redshift galaxies. The emission luminosity of [C II]-157.741 μm transition as a potential tracer for neutral H I gas mass is explored. The [C II] line emission from galaxies in the range $z \approx (1.6, 3.7)$ is studied using absorption-selected QSO whose sightline passes through DLAs. 83 QSO-DLA spectroscopic data was obtained from X-shooter and HIRES spectrograph and some were fitted with Voigt profile using `VoigtFit`. The results were used to find a relationship between the luminosity $L_{[\mathrm{C\,II}]}$ and the gas mass $M_{\mathrm{H\,I}}$. Using the [C II]-to-H I relation, $\log \beta_{[\mathrm{C\,II}]}$, it is found that $\log \beta_{[\mathrm{C\,II}]}$ is decreasing as a function of impact parameter. Further analysis on the metallicity dependence of $\log \beta_{[\mathrm{C\,II}]}$ shows a decreasing trend as metallicity increases. The metallicity-$\log \beta_{[\mathrm{C\,II}]}$ relation was compared to Gamma Ray Burst data from Heintz et al. (2021). The linear regression of the $\log \beta_{[\mathrm{C\,II}]}$ as function of metallicity for QSO is shown to be decreasing linearly with a similar slope but a factor of 10 higher than GRB relation for all $N(\mathrm{H\,I})$. It was then concluded that the usage of QSO sightlines to probe H I using [C II] emission as a tracer is not feasible.

Populärvetenskaplig beskrivning

75 % of the Universe's baryonic content consists of hydrogen (H) and is the main component of galaxy composition making it an important gas in galactic processes. In high-red shifted galaxies, the concentration of neutral hydrogen as a function of galactic radius is still an open research question. Detection of elements in galactic gas clouds is done by performing spectroscopy. The current method of measuring hydrogen is done using the 21 cm hyperfine transition of H I, however it can only be directly observed inside galaxies at moderate distances. Hence other efficient methods to trace H I needs to be developed. One suggested method is to use the emission of the fine structure transition of singly ionised carbon [C II]. The emission of this line can be measured using the absorption spectrum of quasar sightlines passing through the outer edges of large elliptical Damped Lyman Alpha's (DLA) galaxy counterparts.

Quasars are active galactic nuclei that emit broad-spectral profile due to morphology of the object. Quasars are brightest object in the universe and the most powerful of them can easily outshine their host galaxies some even being bright enough to be measured easily across most of the observable universe. Their emitting region being no bigger than our own solar system. The broad-spectral profile of a quasar covers gamma rays to radio waves, hence covering vast regions of the electromagnetic spectrum. This is advantageous because anything in the line of sight of a quasar will be visible through the absorption in the quasar's emission spectrum. Hence performing spectroscopy on the quasar is advantages due to its brightness and the breadth of the emission spectrum.

Using spectroscopy, ratio of [C II]-to-H I using line profile can be derived. A conversion factor can be then identified between Hydrogen and single ionised Carbon. This would provide a direct calibration of [C II]to HI in high-redshift galaxies, opening the possibility to determine the HI gas mass with [C II] of the most distant galaxies that are otherwise too faint to be detected with 21 cm hyperfine transition observations.

This project uses imaging data from the Hubble Space Telescope and spectroscopic data from the X-shooter spectrograph mounted on the ESO Very Large Telescope in Chile. Python libraries such as Astropy, PetroFit are used for photometric analysis to determine the galactic properties of DLA. Using a program, developed in Copenhagen University's Niels Bohr Institute, called `VoigtFit`, spectral analysis of line profiles can be performed to determine the [C II]-to-H I ratio. This research is to compliment H I density developed using Gamma Ray Burst sightlines that penetrate the inner region with quasar sightlines that penetrate the outer regions of the DLAs. If the proposed theory proves correct with factual evidence, this will open new doors to understanding baryonic density in early galaxies alongside the star formation rate as a function of galactic radius.

Contents

Chapter 1

Introduction

Since the Big Bang, baryons have collapsed along with dark matter to form structures of large scale such as stars and galaxies. Overtime their mass would increase which led to further collapse of gas. However only a minority of the baryonic gas inflow is stored in stars. Cooling of dense H I gas formed from the recombination of protons and electrons forms molecular clouds of H_2 and is shown to be a strong causation for star formation (Glover & Clark 2012). The neucleosynthesis in stars as first described in Burbidge et al. (1957) increases the overall metallicity of the galaxy via stellar feedback. Since star formation is closely related to the H I and H_2 gas density (Wolfire et al. 2003), they can be used as tracers for star formation. Therefore studying the abundance of these species is essential for studying the evolution of galaxies through changes in star formation and metallicity. Two main methods used to study the elemental abundances in high redshift galaxies is by using QSO or GRB sightlines that pass through clouds of gas in the galaxies. This report focuses on the feasibility of using QSO sightlines to measure the [C II] to H I connection in high redshift absorption-selected galaxies.

1.1 QSO-DLA

Quasi-stellar objects (QSO) or quasars for short are the brightest objects in the universe with distinct broad-band emission. They are the most powerful of the Active Galactic Nuclei types which contains a super massive black hole in the center of the host galaxy (Sparke & Gallagher 2010). The emissions originate from the relativistic accretion matter around the black hole, an area as small as the solar system but with luminosity easily exceeding $L > 10^{12} L_{\odot}$ (Sparke & Gallagher 2010; Elvis 2000). The structure of the quasar can be seen in figure 1.1 as presented by Elvis.

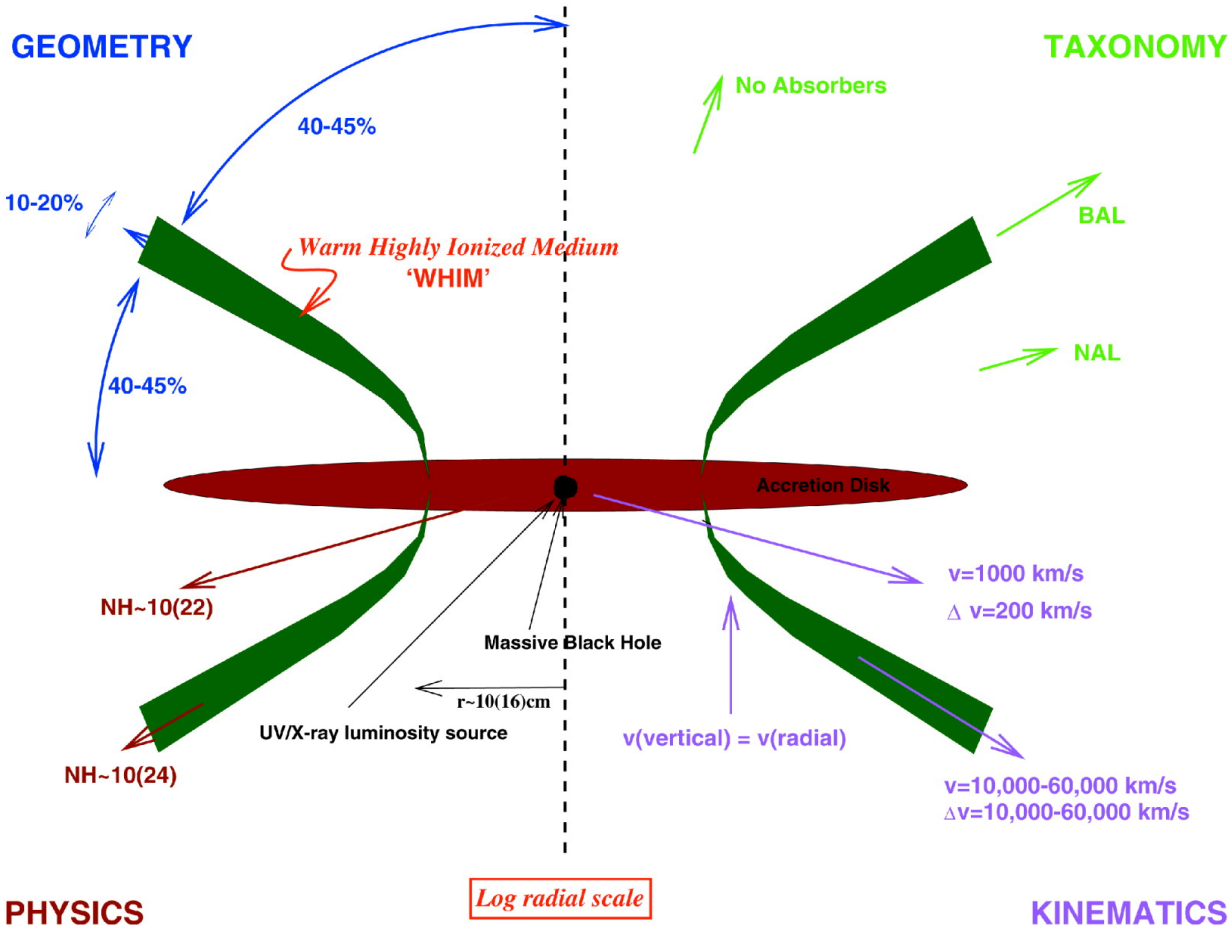

Figure 1.1: Structure of a Quasar (Elvis 2000)

The figure is constructed such that it explains the Broad Emission Line Regions (BELR). The top right of figure 1.1 shows the taxonomy which show the different absorption features depending on the different line of sight. The Warm Highly Ionised Medium (WHIM) gives rise to the Broad Absorption Lines (BAL) and the line of sight near the accretion disk gives rise to the Narrow Absorption Line (NAL). The bottom right of figure 1.1 shows the expected velocities of the quasar structure. The bottom left of figure 1.1 shows the typical H I column densities. Finally, the top left shows the angles that is required to produce the emission features typically seen (Elvis 2000).

Relativistic Doppler Broadening is responsible for the broadening of the emission lines from the different regions the quasar. The radial velocity Δv is notably smaller in the NAL region as compared to BAL region due to the angle made by the intrinsic rotation velocity v of the WHIM with respect to the line of sight.

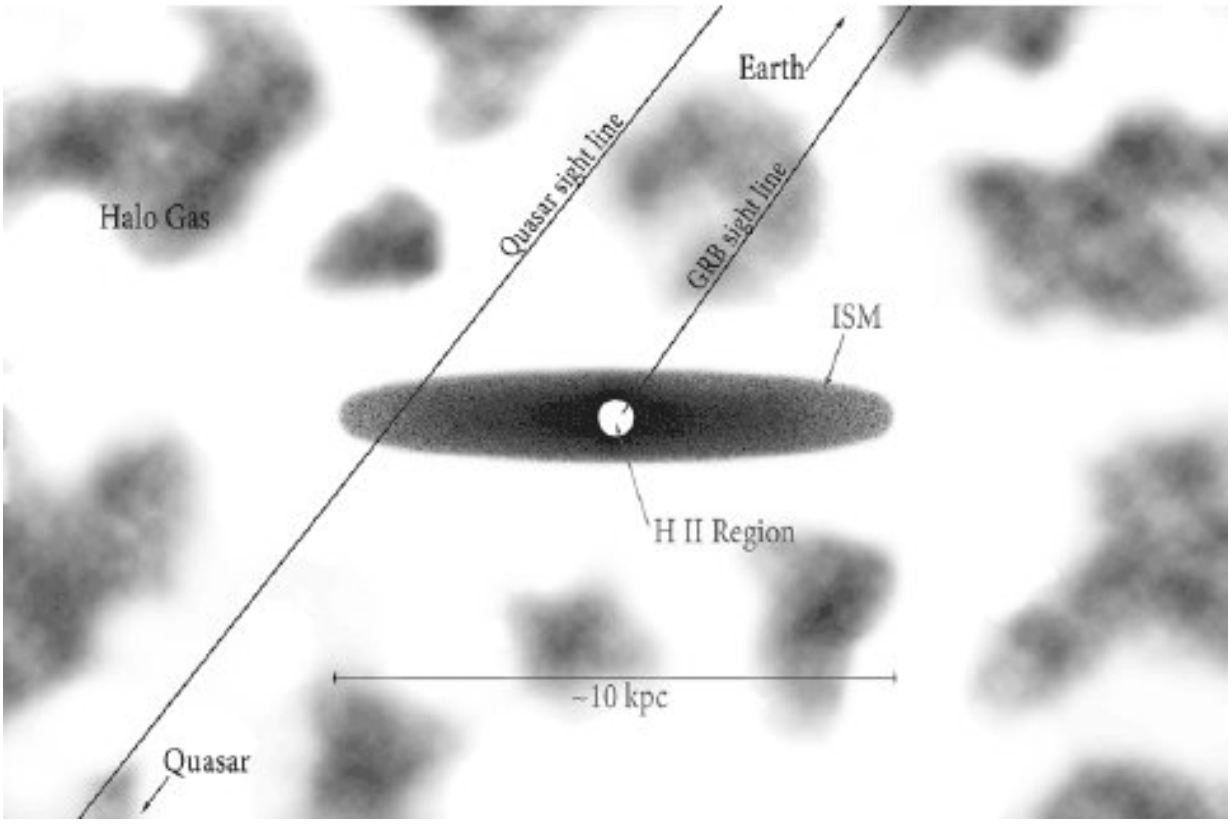

Figure 1.2: QSO and GRB Sightlines passing through a galaxy at different impact perameter (Prochaska et al. 2008)

When the emission sightlines of the QSO pass through diffuse Interstellar Medium (ISM), absorption features of atomic and molecular transitions in the gas can be seen in the emission spectrum at lower redshifts. The absorbing material is a mixture of hydrogen, helium and heavier elements produced in stellar neucleosynthesis. The column density $N(\mathrm{X})$ of elemental ion X is the number density along the sightline around a redshift z of the gas cloud. A Damped Lyman-α (DLA) is an absorber system that has $N(\mathrm{H\,I}) > 2 \times 10^{20}\,\mathrm{cm}^{-1}$ (Wolfe et al. 1986). In the redshift interval up to $z \approx 5$, DLAs contain the dominant neutral H I mass of the universe (Wolfe et al. 2005). Furthermore, around redshifts $z = [3.0, 4.5]$, DLA's contain substantial H I gas mass to be responsible for the large fraction of visible stellar mass in present day galaxies (Storrie-Lombardi & Wolfe 2000). This led to the belief that DLAs, at high redshifts, serve as important H I reservoirs for star formation, which has also been proven with cosmological simulations to be accurate (Nagamine et al. 2004). DLAs are easily identifiable by the absorption of Lyman-α 1215.7 Å transition of H I ($n = 2 \rightarrow n = 1$) in the emission spectrum of background sources with protrusive damping wings (Kramida 2010). Similar to QSOs, Gamma-ray bursts (GRB) are another example of background source that act as a powerful cosmic probes to study different gas-phase elements in the interstellar medium (ISM) of the host galaxy (Schady 2017). Since they are a result of core collapse supernovae of massive stars (Woosley &

Bloom 2006), they can be used as a trace of star formation history (Robertson & Ellis 2012). Most spectra of GRB afterglows contain in them the Lyman-α 1215.7 Å transition of H I in the line of sight (Fynbo et al. 2009); which is rational considering the fact that a GRB forms in the regions of high star formation with high neutral gas density. It is to be noted that a study to measure the [C II] to H I connection in high redshift absorption-selected galaxies using GRB sightlines was done in Heintz et al. (2021).

QSO and GRB sightlines hence can be used to probe different parts of a galaxy as seen in figure 1.2. Since the GRB form in star forming regions they are more likely to be formed in the central regions of a galaxy while the QSO sightlines have a higher chance of intercepting the external regions of the galaxy. The impact parameter $\mathcal{B}$ of GRBs are significantly lower than the $\mathcal{B}$ for QSO. An impact parameter $\mathcal{B}$ is defined as the shortest distance of the sightline to the center of a galaxy.

DLAs also contain strong low ionisation metals, such as Si II or Fe II, which are provided by metal enrichment from supernovae, which are also found in the neutral gas disks of present day galaxies. High ionisation metal lines such as CrIV or SiIV are characteristic of hot diffuse gas found around galactic halos in modern day galaxies (Ganguly et al. 2005; Fox et al. 2007). [C II*]-1335.708 Å ,with a transition probability $A_{[\mathrm{C\,II}^*]} = 2.89 \times 10^{-8}\,\mathrm{s}^{-1}$, absorption line of singly ionised carbon ($^2P_{\frac{3}{2}} \rightarrow {}^2D_{\frac{5}{2}}$) in the QSO emission spectrum indicates the presence of far UV photons in the DLA gas cloud (Li et al. 2021). These photons are produced by star formation further supporting the theory of DLAs being an excellent source of star formation (Sparke & Gallagher 2010).

1.1.1 Metallicity

The gas metallicity measured with the elemental ion X is given as

$$[\mathrm{X/H}] \equiv \log(\mathrm{X/H}) - \log(\mathrm{X/H})_\odot$$

where $\log(\mathrm{X/H})_\odot$ is the relative density of element X with respect to the density of H in the sun. Different solar elemental abundance is provided by Asplund et al. (2009). It is to be noted that metals in DLAs such as Zn, P and O are better indicators of gas metallicity as compared to Mn, Fe and Cr due to strong dust depletion effects (Cia et al. 2016).

1.2 [C II] as a Tracer for H I

The H I 21 cm hyperfine transition is a well known tracer for neutral hydrogen gas (Hoppmann et al. 2015). As a consequence of the weakness of the hyperfine transition, observation of this transition is not practical beyond $z \approx 0.38$ for individual galaxies due to high integration times (Fernández et al. 2016). The lack of a permanent dipole in the H_2 molecule that is cold makes detection close to impossible. Tracers such CO (Tacconi et al. 2010), [CI] (Papadopoulos et al. 2004), dust (Magdis et al. 2012) and finally [C II] (Zanella et al.

2018) have all been employed in tracing molecular gas phase hydrogen. Due to the crucial importance of H I in galactic evolution and the impracticability of 21 cm observations beyond the low redshifts, a powerful tracer needs to be developed.

Similar to CO and [C I], a calibration can be developed for high-redshift galaxies using the fine structure [C II]-157.741 μm transition with a transition probability $A_{[\mathrm{C\,II}]} = 2.29 \times 10^{-6}\,\mathrm{s}^{-1}$ (Kramida & Haris 2022).This transition, ${}^2P_{\frac{3}{2}} \rightarrow {}^2P_{\frac{1}{2}}$, is often very visible and bright enough to be detected at high redshifts and originating from cold and neutral gas. The [C II] transition can be alternatively calibrated to H I rather than above stated H_2 gas mass. Although the transition has been used as a tracer for H_2, simulation and observations show that H_2 gas only contributes little to the overall brightness of the [C II]-157.741 μm (Pineda et al. 2014; Ramos Padilla et al. 2021; Olsen et al. 2021; Tarantino et al. 2021). The relationship between [C II]-157.741 μm transition and neutral or ionised gas is evident in the length in which the emission region is bigger than the star forming, dust and CO regions. A large amount of [C II] is hypothesised to have originated from the extended intergalactic disks of galaxies. The [C II] to H I calibration ratio will be derived purely based on observations rather than assumptions and scaling relations. This does *not* require the [C II] transition gas to be related physically or to a great extent with the H I gas. It merely seeks to provide an abundance ratio between the two transitions in the interstellar medium (Carniani et al. 2018; Fujimoto et al. 2019; Matthee et al. 2019; Harikane et al. 2020; Herrera-Camus et al. 2021).

1.3 Line Profile

If it is assumed that the state of the medium is defined distinctively by the temperature T and the column density N then the absorption lines are well described by a Voigt profile H (Hjerting 1938). It is a convolution between a Lorentz distribution (which describes the natural line broadening of the transition) and a Gaussian distribution (produced by turbulent and thermal motion of the medium) and is mathematically known as a Voigt–Hjerting function. Absorption line profiles that diverge from a Voigt profile will be due to kinematic properties of the medium such as rotation or local turbulent velocity dispersion and broadening which is not due to the overall doppler effect (García 2006).

If an element X undergoes a absorption transition i, then the absorption line profile can be described by the optical depth τ of the transition. If the atomic specifications, such as line strength f_i, damping constant Γ_i and transition wavelength λ of ith transition, is known then the optical density can be defined as

$$\tau_{\mathrm{X}}(\lambda) = K_i N(\mathrm{X}) a_i H(a_i, x(\lambda)) \tag{1.1}$$

where the constants $a_i \equiv \frac{\lambda_i \Gamma_i}{4\pi b}$ and $K_i \equiv \frac{e^2\sqrt{\pi} f_i \lambda_i}{m_e c b}$ (Krogager 2018; García 2006). The relationship between f_i and the transition Einstein A coefficient can be found in Wahlgren (2010). The elementary charge e and the electron mass m_e is obtained from the CODATA recommended values from 2018 (Tiesinga et al. 2021). While the broadening parameter b is to be approximated for the individual components of a absorption line profile. b is a combination of Doppler and turbulent broadening. A line profile of a single component is given the Voigt-Hjerting function:

$$H(a_i, x(\lambda)) = \frac{a_i}{\pi} \int_{-\infty}^{\infty} \frac{e^{-y^2}}{(x-y)^2 + a_i^2} dy. \tag{1.2}$$

It is to be noted that $x_i(\lambda) = \frac{\lambda - \lambda_i}{\lambda_D}$ is the rescalling wavelength where $\lambda_D = \frac{b\lambda_i}{c}$. Equation 1.2 integrates over all possible velocities of the absorbing atom with respect to the observers line of sight, $y = \frac{v}{b}$ (Krogager 2018). It is to be noted that the equation 1.2 is a very computationally gruelling to perform multiple iterations to evaluate each fit. The function can be approximated analytically to be

$$H(a_i, x) \approx H_o - \frac{a_i}{x_i^2} \left[H_o^2 \left(4x_i^4 + 7x_i^2 + 4 + 1.5x_i^{-2} \right) - 1.5x_i^{-2} - 1 \right] \tag{1.3}$$

where $H_o = e^{-x^2}$ (García 2006). Furthermore, equation 1.3 is independent of velocity along the line of sight hence reducing the computation effort by one dimension. The total optical depth is the sum of all the optical depths of the individual components and transitions (Krogager 2018). The total normalised transmittance is then given as

$$I(\lambda) = e^{-\tau(\lambda)}. \tag{1.4}$$

Equation 1.4 is used to fit absorption spectra of QSO-DLA. Along with the fitted $\tau(\lambda)$ and equation 1.3, the value for the column density can be derived using 1.1. The total transmittance profile is however not the observed transmittance profile on the detector. The resolution of the instrument also plays a role in the shape of the spectrum. To fit the observed transmittance $\mathcal{M}(\lambda)$, the intrinsic transmittance in equation 1.4 needs to be convolved with Line Spread Function LSF

$$\mathcal{M}(\lambda) = C(\lambda) \left[I(\lambda) * \mathrm{LSF} \right] \tag{1.5}$$

where LSF was assumed to be a Gaussian whose full width half maximum equal to the spectral resolution and $C(\lambda)$ is Chebyshev polynomial used to normalise the spectrum. If the spectrum is normalised then $C(\lambda) = 1$ and equation 1.5 is fitted to the spectrum.

Chapter 2

Data

2.1 Preliminary Analysis

Initial data analysis was done on QSO Q0918+1636, a well known QSO with a DLA counterpart (Fynbo et al. 2013). A photometric analysis to identify galactic properties of the DLA counterpart was performed. An image was captured by the Hubble Space Telescope (HST) in the IR F160W filter with a 50 s exposure time. It can be seen in figure 2.1 that there exists a very bright object in the center which is identified to be Q0918+1636 and the DLA of interest is the galaxy to the bottom right of the QSO. The axis of the figure represent the pixel number of the on-board CCD (charge coupled device). A 10x10 pixel area of figure 2.1 where there are no sources was used to estimate the background noise. Using the averaged noise value, figure 2.1 was segmented with the condition that pixels inside the segment have a higher count value as compared to the background noise. The pixel coordinate of the QSO sightline and the center of the absorbing galaxy was found by using the global maximum of the segmented objects. The separation between the global maximum of the segmented image was measured in arcseconds, and was converted to proper distance using Planck 2018 cosmology (Planck Collaboration et al. 2020). A preliminary redshift of the DLA was obtained from Fynbo et al. (2011) at $z = 2.5832$, using which it was measured that the impact parameter $\mathcal{B} = 16.297\,\mathrm{kpc}$.

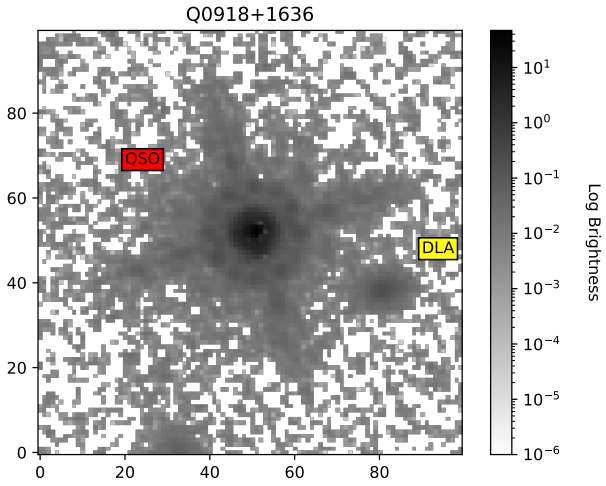

Figure 2.1: HST Image taken in the IR F160W filter with the QSO and it's DLA counterpart

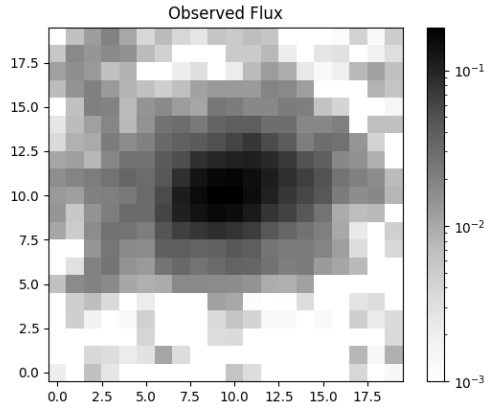

(a) Cutout of the identified DLA from figure 2.1

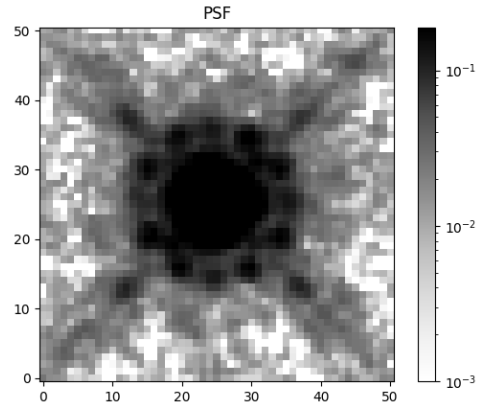

(b) Point spread function of the CCD

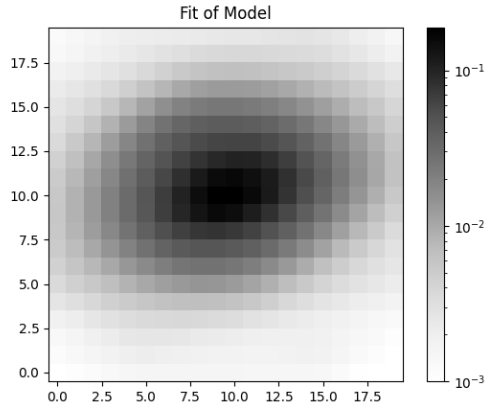

(c) Best fit Sérsic profile

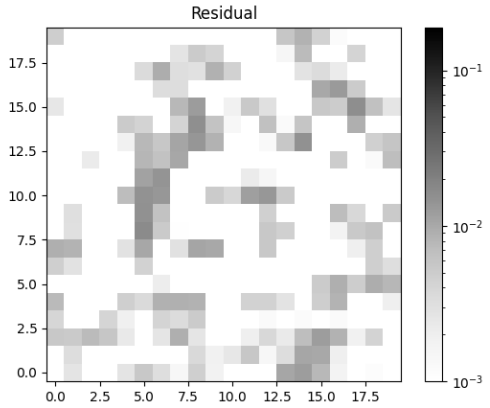

(d) Observed DLA flux subtracted from Sérsic fit

Figure 2.2: Photometry of Q0918+1636

The observed flux in figure 2.2a was convulved with a point spread function (PSF) in figure 2.2b to obtain a true image without instrumental distortion. The true image was then fitted to a Sérsic profile as described in Sersic (1968) and Graham & Driver (2005), with the optimisation of the parameters of the Sérsic profile done with chi square minimisation. A model was then produced as seen in figure 2.2c with its residual seen in figure 2.2d. Figure 2.2c's measured effective radius is 1.44 ± 0.21 kpc and the total AB magnitude of 21.56.

Since figure 2.2 confirmed the existence of a galaxy counterpart to the DLA, a spectrum can now be obtained and studied for absorption features. To study the characteristics of the DLA no photometry is required. The DLA does not necessarily have to be part of a galaxy. The definition is purely a spectroscopic characteristic. However for the sake of this report, the DLAs investigated must have a galaxy counterpart. Since the spectroscopy was performed on the X-shooter medium resolution echelle spectrograph (Richards et al.

2001; Vernet et al. 2011). It is secured onto unit 2 of the the Very Large Telescope (VLT) in Chile's Paranal observatory and is managed by European Southern Observatory (ESO). The light entering the instrument is split in three and each go through one of the spectrographs known as arms. The wavelength range can be seen in table 2.1.

Table 2.1: Arm properties of the X-shooter

Arm	λ-range [Å]	Slit Width [″]	Slit Length [″]	Nominal Resolution
UVB	3000-5500	1.3	11	4000
VIS	5500-10000	1.2	11	6700
NIR	10000-25000	1.2	11	4300

The resolution of the X-shooter is set either by the seeing disk diameter or the slit width. If the seeing is smaller than the slit width then the nominal resolution is no longer valid (Krogager et al. 2017). However if the seeing is wider than the slit width, then the resolution is set by the slit gratings.

For slit widths that are larger than the seeing, there is a inverse relationship between the seeing and the effective resolution. The seeing disk is measured on the day of observation and using the relationship found by Selsing et al. (2019), the VIS and NIR arm resolution can be determined. The relationship between the seeing and the effective VIS resolution is described by the linear relationship $a \times S + B$ where S is the seeing in arcsec, $a = 25.2 \pm 0.8\,\mathrm{km/s}$ and $B = 3.8 \pm 0.7\,\mathrm{km/s}$. Since there is no UVB atmospheric transitions, to calculate the UVB arm resolution a simple scaling can be performed from the VIS resolution by taking the the ratio of the effective VIS resolution and the nominal VIS resolution multiplied by the nominal UVB resolution. Table A.1 of appendix A contains the QSOs and their effective resolutions calculated using the prior relationship. The raw spectrum from VIS and UVB band were analysed using `VoigtFit` for absorption features.

2.2 Method

`VoigtFit` is a Voigt profile fitting program developed by Krogager. The user is required to provide the program with information about the DLA of interest in a parameter file. The information initially includes initial redshift guess of the DLA, spectrum files from the different arms, the corresponding resolutions and a strong transition to be manually fit. The redshift z was initially guessed by finding the center by eye of the very prominent Lyman-α transition.

Then a interactive plot appears where the user was required to select the number of components, then mask out the regions that should not be included for the Chebyshev polynomial fitting to normalise the spectrum. It is now to be noted that the spectra of Q0918+1636 was already normalised for dust extinction and quasar broad line emission profile. Therefore no Chebyushev polynomial fitting was required and was set to unity in equation 1.5. The masking was also performed to mask regions of the continuum flux that was not required to be included in the fit.

Once the fitting for one strong transition was completed, an output .fit file was produced. It contained the broadening parameter and the redshift of the individual components. These components were copied back into the parameter file and the b and z were set to constant. The systematic redshift of the DLA was reset to redshift of the largest component of the DLA. This transition shall hence be known as the resolution transition. The redshift of the largest component of the resolution transition is also the systematic redshift of the system.

More metal transitions were added to the parameter file to be fitted with the components that were identified from the resolution transition. After more masking was completed for the additional transitions, an updated .fit file was produced. Now using these metal lines as a constraint on the fitting, the relevant C^+ transition were fitted. It is to be noted that masking was performed with care on these the relevant C^+ transition due to the lower resolution of the UVB arm compared to the VIS and the high saturation of the lines.

Finally once the relevant C^+ transition lines were fitted, only using the systematic redshift component and by letting b vary, the H I Lyman-α transition was fitted. Then by copying the component of the H I into the parameter file and using the rest of the fitted lines, the whole spectrum was together fitted. This process was repeated several times, each time altering the masking until a result with lowest uncertainty on the column density was achieved.

Finally three files are produced that are important for the project: .fit contains the column density N and broadening parameter b of the individual component, .pdf which contains the images of the spectrum with the individual fits and finally .cont which contains the Chebyshev polynomial coefficients which was found with chi square minimisation.

Chapter 3

Results

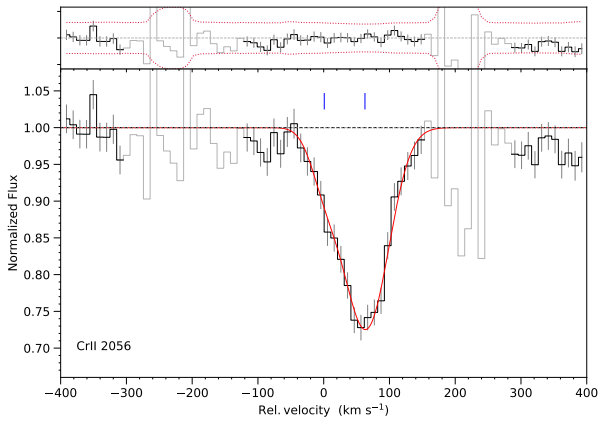

Figure 3.1: Q0918+1636 Cr II transition

For the resolution transition, Cr II − 2056 Å was selected to be used to identify the components, redshift and broadening of the DLA of Q0918+1636. Figure 3.1 shows how `VoigtFit` was used to fit absorption line profile onto the transition. The red curve is the line profile fitting and the blue dash on top of the line profile mark the components present in the system. The components and the related parameters are shown in table 3.1.

As described above, the components were used to constrain the fit for [C II*] transition and other metal lines as seen in in figure 2.1 in appendix D.1.

Table 3.1: Components of the resolution transition of Q0918+1636

Ion (X)	Component	Redshift (z)	Broadening parameter (b) [km/s]
Cr II	1	2.5822	44.93±3.82
	2	2.5817	44.93±3.43

The constrained fit of [C II*] is shown in figure 3.2a. It is noted that CIIa is the [C II*] transition of interest in figure 3.2a. This line is saturated along with the nearby C II transition and shows the importance of constraining the fit with a resolution wavelength.

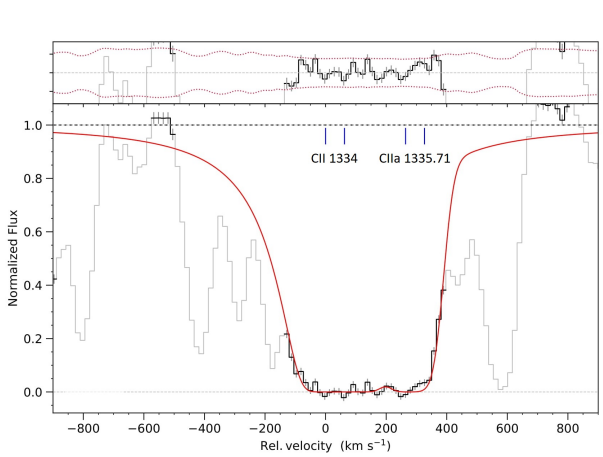

(a) Q0918+1636 C II transitions

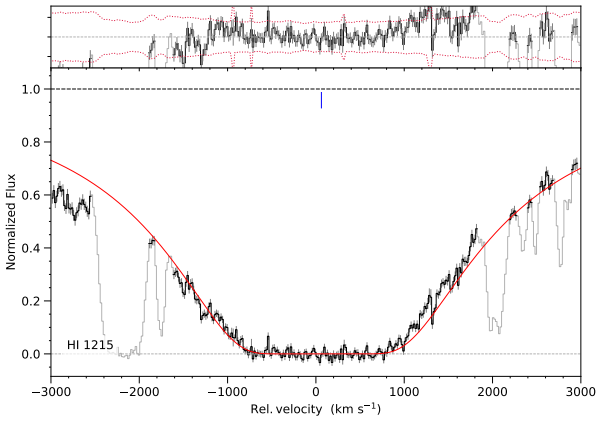

(b) Q0918+1636 Lyman α Transition with the damping wings

Figure 3.2: Q0918+1636 line profiles used to measure column density

From the table 3.1, the system's redshift can be calculated to be $z = 2.582$ which is precisely what is measured to be in Fynbo et al. (2011). The derived column densities of figure 3.1, 3.2, and D.1 can be found in table 3.2. The metallicity using Zn II transition is measured to be $[\mathrm{Zn/H}] = -0.356 \pm 0.045$.

Table 3.2: Derived column densities of metals in Q0918+1636 sightline

Ion (X)	Column Density ($\log(N(\mathrm{X}))$) [$\log(\mathrm{cm}^{-2})$]
H I	21.067±0.006
[C II*]	14.959±0.059
Mn II	13.462±0.022
Ni II	14.395±0.023
Si II	15.838±0.023
S II	15.993±0.022
Zn II	13.341±0.018
C II	19.547±0.059

A calibration has to be performed now to convert from column density of H I and [C II*] to H I gas mass per unit [C II] transition emission luminosity. Since there is relatively low density of transitioning C II gas, it is valid to only consider spontaneous emission and neglect stimulated emission and absorption. Therefore only the Einstein A coefficient of [C II] transition is required for the rate equation $\frac{dN_{[\mathrm{C\,II}]}}{dt}$. The population on the upper level ${}^2P_{\frac{3}{2}}$ of [C II] is given by number of [C II*] transitions. As seen in figure 3.3, [C II*] transition lower level is the same as the upper level of [C II].

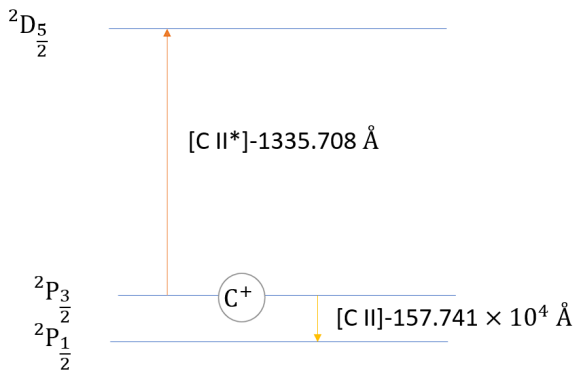

Figure 3.3: C^+ gas transitions

The rate equation $\frac{dN_{[\mathrm{C\,II}]}}{dt}$ of the population on the upper level $^2P_{\frac{3}{2}}$ is given by

$$\frac{dN_{[\mathrm{C\,II}]}}{dt} = A_{[\mathrm{C\,II}]} N_{[\mathrm{C\,II}^*]} \tag{3.1}$$

where $N_{[\mathrm{C\,II}^*]}$ is the number of [C II*] transitions (Foot 2005). The luminosity $L_{[\mathrm{C\,II}]}$ of [C II] transition is given by the energy of the transition multiplied by the rate of the transition as

$$L_{[\mathrm{C\,II}]} = \frac{hc}{\lambda_{[\mathrm{C\,II}]}} \frac{dN_{[\mathrm{C\,II}]}}{dt} = \frac{hc}{\lambda_{[\mathrm{C\,II}]}} A_{[\mathrm{C\,II}]} N_{[\mathrm{C\,II}^*]} \tag{3.2}$$

where $\lambda_{[\mathrm{C\,II}]} = 157.741\,\mu$m (Kramida & Haris 2022). The number of H I with atomic mass $m_{\mathrm{H\,I}}$ from the total gas mass $M_{\mathrm{H\,I}}$ is $N_{\mathrm{H\,I}} = \frac{M_{\mathrm{H\,I}}}{m_{\mathrm{H\,I}}}$. Rewriting equation 3.2 in terms of $N_{[\mathrm{C\,II}^*]}$ and dividing by $N_{\mathrm{H\,I}}$

$$\frac{N_{\mathrm{H\,I}}}{N_{[\mathrm{C\,II}^*]}} = \frac{M_{\mathrm{H\,I}}}{L_{[\mathrm{C\,II}]}} \frac{\frac{hc}{\lambda_{[\mathrm{C\,II}]}} A_{[\mathrm{C\,II}]}}{m_{\mathrm{H\,I}}}.$$

Rewriting it in terms of $\beta_{[\mathrm{C\,II}]} \equiv \frac{M_{\mathrm{H\,I}}}{L_{[\mathrm{C\,II}]}}$ and changing the units to $\left[\frac{M_\odot}{L_\odot}\right]$

$$\beta_{[\mathrm{C\,II}]} = \frac{m_{\mathrm{H\,I}}}{\frac{hc}{\lambda_{[\mathrm{C\,II}]}} A_{[\mathrm{C\,II}]}} \frac{N_{\mathrm{H\,I}}}{N_{[\mathrm{C\,II}^*]}} \frac{3.839 \times 10^{33}\,\mathrm{ergs/s}}{1.989 \times 10^{33}\,\mathrm{g}}. \tag{3.3}$$

The value for Planck constant h and speed of light in a vacuum c is given by CODATA recommended values from 2018 while the conversion to solar units is dictated by the values recommended by International Astronomical Union in 2015 (Tiesinga et al. 2021; Mamajek et al. 2015). The evaluated relationship for equation 3.3 is given by

$$\beta_{[\mathrm{C\,II}]} = 1.117 \times 10^{-4} \frac{N_{\mathrm{H\,I}}}{N_{[\mathrm{C\,II}^*]}} \left[\frac{M_\odot}{L_\odot}\right] \tag{3.4}$$

In the case of QSO sightlines, the number of transitions N can also be in the form of number density per unit area [cm^{-2}] (column density). Hence when the column density is measured along a QSO-DLA sightline, $\beta_{[\mathrm{C\,II}]}$ can be derived. Using equation 3.4, for Q0913+1636 sightline, the measured $\log \beta_{[\mathrm{C\,II}]} = 2.159 \pm 0.084$.

3.1 QSO with known $\mathcal{B}$

The next step was to extend the above work to QSO sightlines that have known impact parameters. Two QSO spectra were measured:Q1313+1414, PKS0458-020. The impact parameter of the two QSO are shown in table A.1 as derived in Krogager et al. (2017).

Q1313+1441

Q1313+1441 has an impact parameter of $\mathcal{B} = 11.4 \pm 1.7\,\mathrm{kpc}$. The spectrum from the VIS and UVB arm was analysed using `VoigtFit` and the absorption line profiles were fitted. A resolution transition $\mathrm{Fe\,II} - 2374\,\text{Å}$ was used to identify the spectral components and the results are shown in table 3.3.

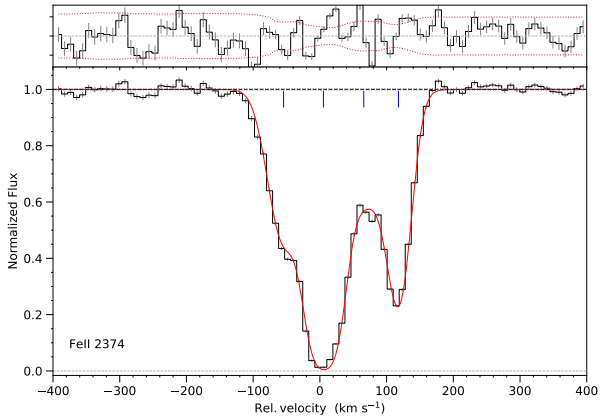

(a) Q1313+1441 Fe II-2374 Å transition

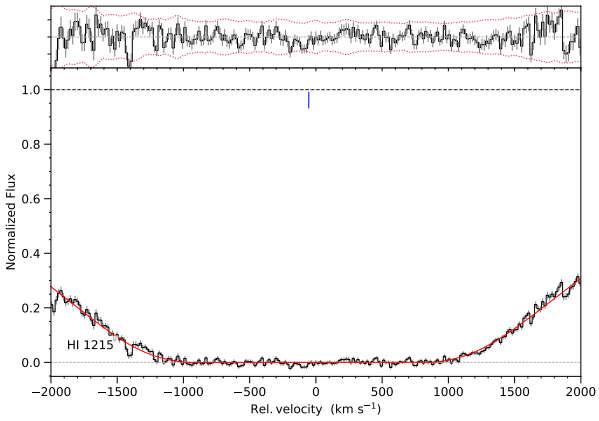

(b) Q1313+1441's Lyman α absorption with the dampening wings

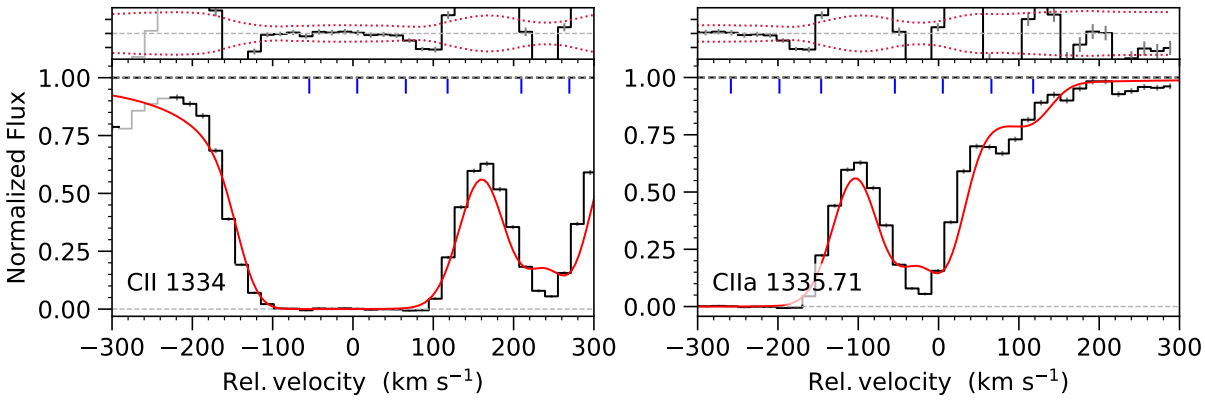

(c) C II transitions

Figure 3.4: Q1313+1441 line profiles used to measure column density

From table 3.3 the redshift of the galaxy counterpart is calculated by taking the weighted average of the redshifts of the individual component, and was measured to be $z = 1.794$. The column densities of the line profils of figure 3.4 and D.2 in appendix D.2 is given in table 3.4.

Table 3.3: Components of the resolution transition of Q1313+1441

Ion (X)	Component	Redshift (z)	Broadening parameter (b) [km/s]
Fe II	1	1.7952	18.12 ± 0.91
	2	1.7948	3.42 ± 441.50
	3	1.7941	9.71 ± 3.01
	4	1.7936	26.77 ± 3.17
	5	1.7945	5.43 ± 335.26

Table 3.4: Derived column densities of metals in Q1313+1441 sightline

Ion (X)	Column Density ($\log(N(\mathrm{X}))$) [$\log(\mathrm{cm}^{-2})$]
H I	21.270±0.040
[C II*]	14.892±0.058
C II	18.884±0.045
Si II	15.838±0.023
Zn II	13.102±0.038

The metallicity of Q1313+1441 using Zn II transition was measured to be [Zn/H] = −0.746±0.065. Using equation 3.4, for the Q1313+1441 sightline, the measured $\log \beta_{[\mathrm{C\,II}]} = 2.423 \pm 0.095$.

PSK0458-020

PSK0458-020 has an impact parameter of $\mathcal{B} = 2.7 \pm 0.3\,\mathrm{kpc}$. The spectrum from only the UVB arm was analysed using `VoigtFit` and the absorption line profiles were fitted. A resolution transition Si II − 1526 Å was used to identify the spectral components and the results are shown in table 3.5. Unlike the previous two QSO spectra, figure 3.6b's [C II*] transition is not saturated.

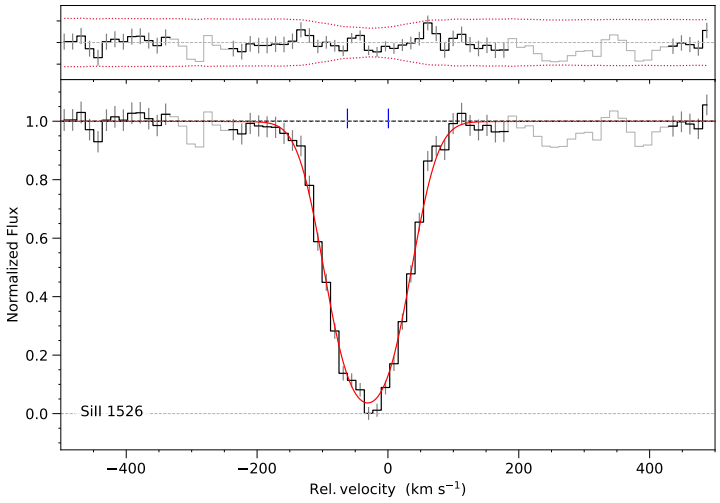

Figure 3.5: PSK0458-020 Si II − 1526 Å transition

From table 3.5 the redshift of the galaxy counterpart is calculated by taking the weighted average of the redshifts of the individual components, and was measured to be $z = 2.039$. The column densities of the line profiles of figure 3.5 , 3.6, and D.3 in appendix D.3 is given in table 3.6.

Table 3.5: Components of the resolution transition of PSK0459-020

Ion (X)	Component	Redshift (z)	Broadening parameter (b) [km/s]
Si II	1	2.0387	15.27 ± 93.87
	2	2.0380	15.64 ± 98.17

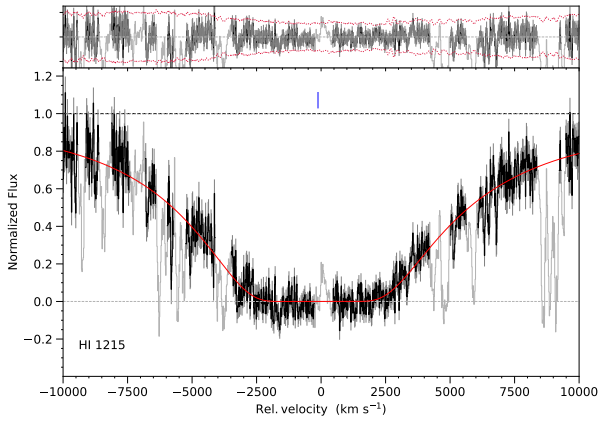

(a) PSK0458-020's Lyman α absorption with the dampening wings

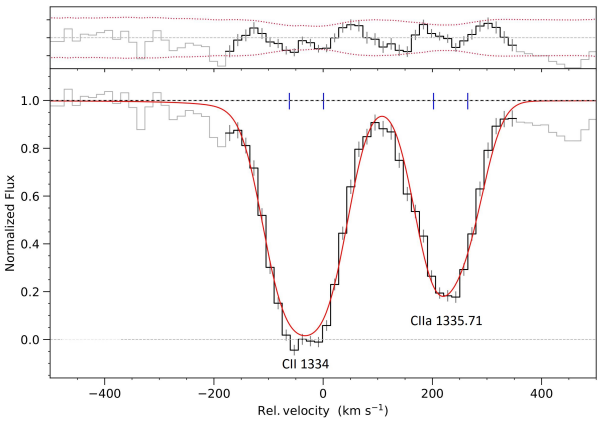

(b) C II transitions

Figure 3.6: PSK0458-020 line profiles used to measure column density

Table 3.6: Derived column densities of metals in PSK0458-020 sightline

Ion (X)	Column Density ($\log(N(\mathrm{X}))$) [$\log(\mathrm{cm}^{-2})$]
H I	21.270±0.040
[C II*]	14.956±0.139
C II	17.785 ± 0.168
Si II	16.175±0.121

The metallicity of PSK0458-020 using the Si II transition was measured to be [Si/H] = −1.279±0.122. Using equation 3.4, for the PSK0458-020 sightline, the measured $\log \beta_{[\mathrm{C\,II}]} = 2.392 \pm 0.197$. As seen in table A.1 in appendix A, the seeing is larger than the slit width, hence the resolution used is the nominal resolution as reported in table 2.1. This is a major reason why the uncertainty is a magnitude larger for spectroscopic properties of PSK0458-020 than to the other QSO spectroscopic values.

QSO PSK0458-020 and Q1313+1441 were only normalised for dust reddening but not for the QSO broad emission features. Hence the normalisation was done by setting the Chebyshev polynomial to the first degree for PSK0458-020 and Q1313+1441. The relevant column densities and DLA system information from the X-shooter can be found in appendix B table B.1. The X-shooter data in table B.1 was fitted using `VoigtFit` as described in section 2.2.

3.2 Larger QSO sample

To evaluate the validity of [C II] emission as a tracer for quasar sightlines, $\beta_{[\mathrm{C\,II}]}$ must be found for more than 3 to QSO sightlines. The data obtained from HIRES Neeleman et al. (2015) already had the QSO's spectrum analysed for the column density of [C II*], H I and

the metalicities of each DLA. It is known from figure 8 of Krogager et al. (2017) that lower impact parameters trace higher H I and vice versa. Hence H I column densities can be used to trace impact parameter. The HIRES data (Neeleman et al. 2015) is found in appendix C table C.1. It is to be noted that some [C II*] line profile from HIRES spectrograph was either too saturated to be detected in which case a lower limit can be theoretically determined using the the broadening parameter and the number of components of a strongly well resolved transition. Similarly in the opposite case of no detection, based on the signal to noise ratio, the broadening parameter and the number of components of a strong well resolved transition; a higher limit on the column density can be theoretically determined. This is shown in the lack of an error and the limit flag column of table C.1.

Chapter 4

Discussion

Using the derived $N(\mathrm{H\,I})$ and $N([\mathrm{C\,II}^*])$, the $\beta_{[\mathrm{C\,II}]}$ was derived using equation 3.4. The figure 4.1 was plotted using HIRES and X-shooter data. Table E.1 contains all the beta values that are plotted in figure 4.1 along with the relevant QSO sightline. It can be seen that there is a larger concentration of data points for lower $N(\mathrm{H\,I})$ as compared to the higher $N(\mathrm{H\,I})$. The lower $N(\mathrm{H\,I})$ is dominated by points with lower bound for $N([\mathrm{C\,II}^*])$.

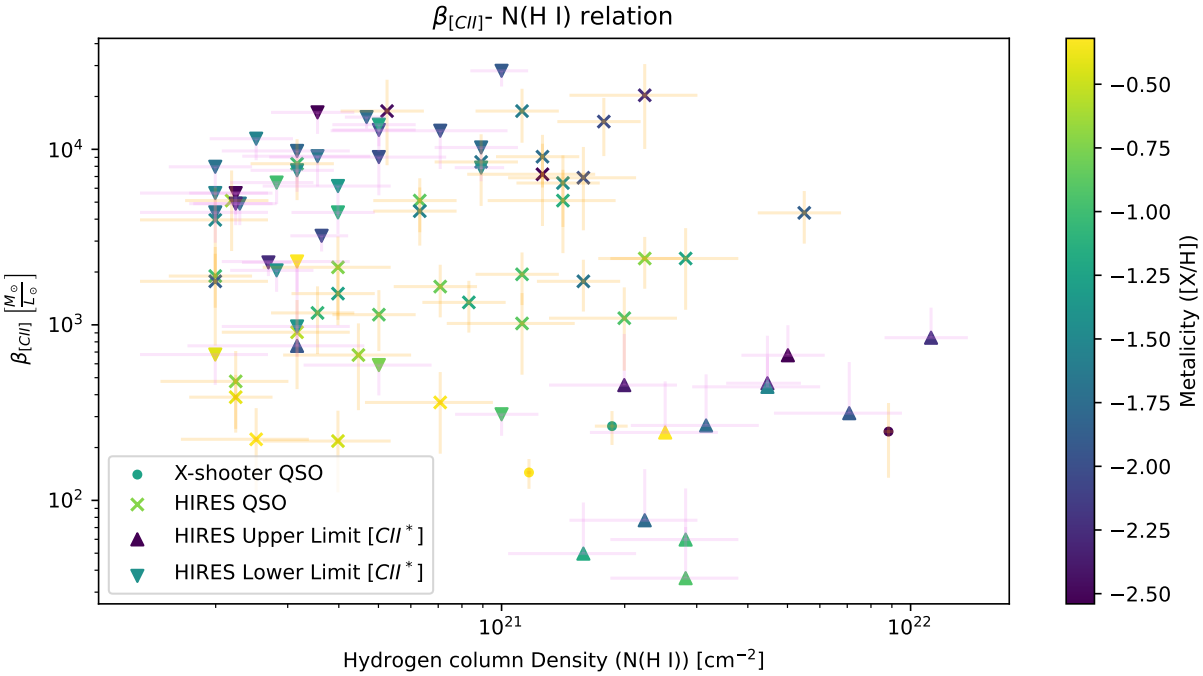

Figure 4.1: $\beta_{[\mathrm{C\,II}]}$ as a function of hydrogen column density

This is an anticipated finding as, according to equation 3.3, $N([\mathrm{C\,II}^*])$ is inversely proportional to $\beta_{[\mathrm{C\,II}]}$. This is also true for the opposite case of the higher bound of

$N([\mathrm{C\,II^*}])$. The blue circles representing X-shooter data lie at higher $N(\mathrm{H\,I})$ but relatively the same value for $\beta_{[\mathrm{C\,II}]}$. The data in figure 4.1 shows a decreasing trend in $\beta_{[\mathrm{C\,II}]}$ for increasing values of $N(\mathrm{H\,I})$. As mentioned in subsection 3.2, if $N(\mathrm{H\,I})$ is used as a tracer for impact parameter (Krogager et al. 2017), then it can be deduced that for higher impact parameters, $\beta_{[\mathrm{C\,II}]}$ increases. But the higher and lower impact parameters are dominated by regions of lower metallicity in figure 4.1 which shows a metallicity dependence on $\beta_{[\mathrm{C\,II}]}$ relation. To understand the metallicity dependence of the $\beta_{[\mathrm{C\,II}]}$, metallicity was plotted as

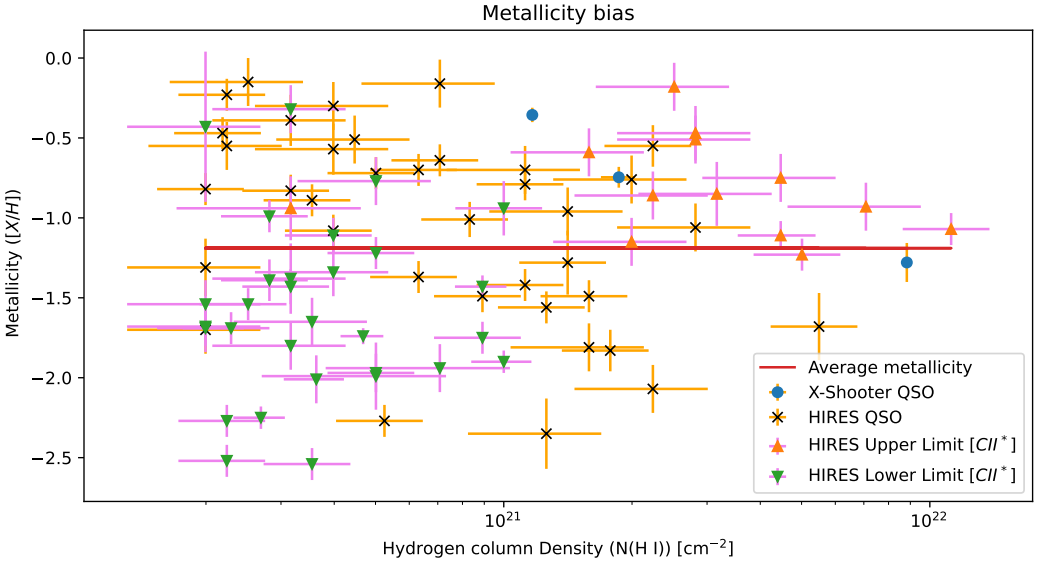

Figure 4.2: metallicity of the gas at different impact parameters

a function of $N(\mathrm{H\,I})$ in figure 4.2 to check for the metallicity distribution for different impact parameter. The red horizontal line represents the average metallicity of the absorption-selected QSO sample: measured to be -1.189 ± 0.067. For lower $N(\mathrm{H\,I})$, higher impact parameters, there is a distribution fairly equally for metalicities over and below the average metallicity. This is due to the fact that different sized DLAs have different star forming region. For a larger impact parameter, the larger DLA will have star forming region that is larger in size as compared to a smaller DLA. This means that larger impact parameters will likely probe a star forming region in in larger DLAs leading to high metallicity along the sightline. While the same impact parameter for the smaller DLA will have it's extended H I gas envelope probed: leading to a lower metallicity. For lower impact parameters, the metallicity is usually higher than the average metallicity of the sample showing a bias towards higher metallicity gas for lower impact parameters. This is because star formation is occurring within the cores of the DLA-galaxy which lead to metal enrichment of the surrounding gas in the star forming region.

To find galaxies whose metallicity is lower than the average, the galaxy should be in the early stages of star formation. The DLA-galaxies would need to be at much higher

redshifts than the ones from table C.1 and B.1. Selection bias also plays a role in the overall absorption-selected QSO sample of HIRES data. It is to be noted that some of the QSO are chosen to be part of the survey based on the strength of their metal lines. This leads to a higher metallicity bias as seen in figure 4.2. Selecting samples based on the $N(\mathrm{H\,I})$ give a better representation of the overall DLA population and would reduce the selection bias (Neeleman et al. 2015, 2013).

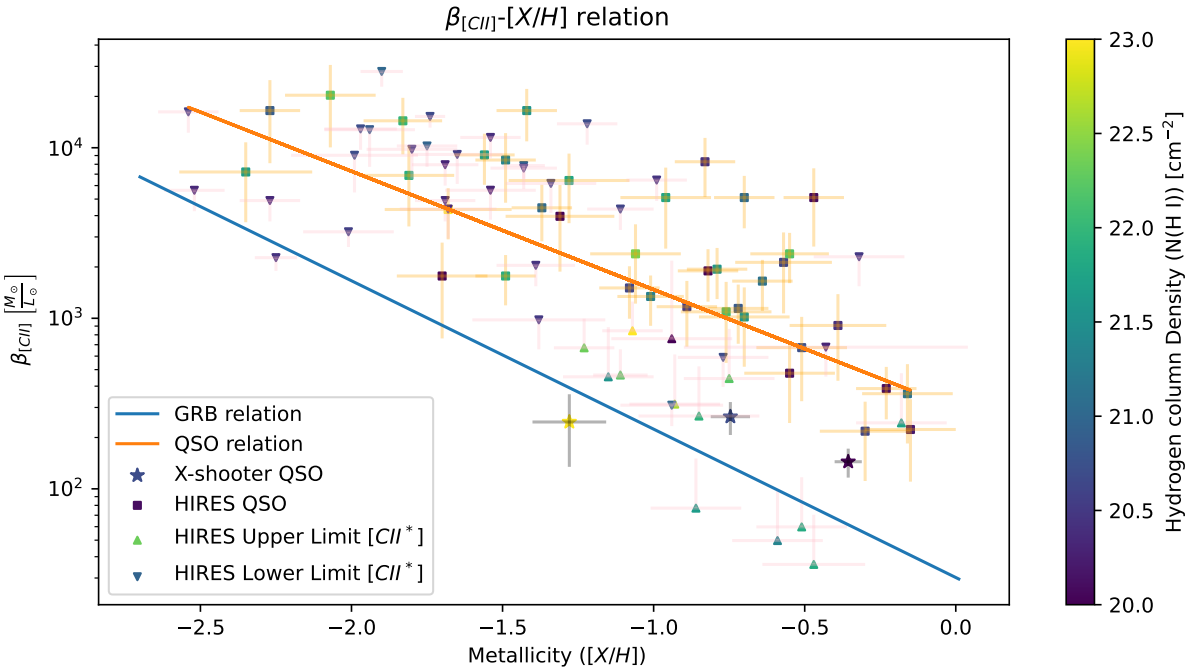

Figure 4.3: $\beta_{[\mathrm{C\,II}]}$ as a function of [X/H] from both HIRES and X-shooter along with the GRB relation found in Heintz et al. (2021)

Figure 4.3 shows $\beta_{[\mathrm{C\,II}]}$ plotted as a function of matalicity using equation 3.4. The colours of the markers represents the $N(\mathrm{H\,I})$. Figure 4.3 contains the linear regression of a similar study conducted by Heintz et al. studying the H I gas abundance and the validity of C II gas as a tracer using Gamma Ray Bursts (GRB) sightlines instead of QSOs (Heintz et al. 2021). A linear relationship

$$\log \beta_{[\mathrm{C\,II}]} = (-0.87 \pm 0.09) \times [X/H] + (1.48 \pm 0.12)$$

was found between the metallicity and $\beta_{[\mathrm{C\,II}]}$ and shall be known as the GRB relation. Similarly, A linear regression was fitted to the QSO data and the following relationship was found

$$\log \beta_{[\mathrm{C\,II}]} = (-0.694 \pm 0.079) \times [\mathrm{X/H}] + (2.474 \pm 0.106).$$

The above relation is plotted along with GRB relation in figure 4.3. This linear relation shall henceforth be called QSO relation. Figure 4.3 contains a swarm of data points right

above the GRB relation with the offset, as measured in figure 4.3, being independent of $N(\mathrm{H\,I})$. The offset between the GRB and QSO value is shown in 4.4. It shows no offset relation that are based on metallicity or impact parameter. However the average QSO value is approximately 10 times greater than the GRB value.

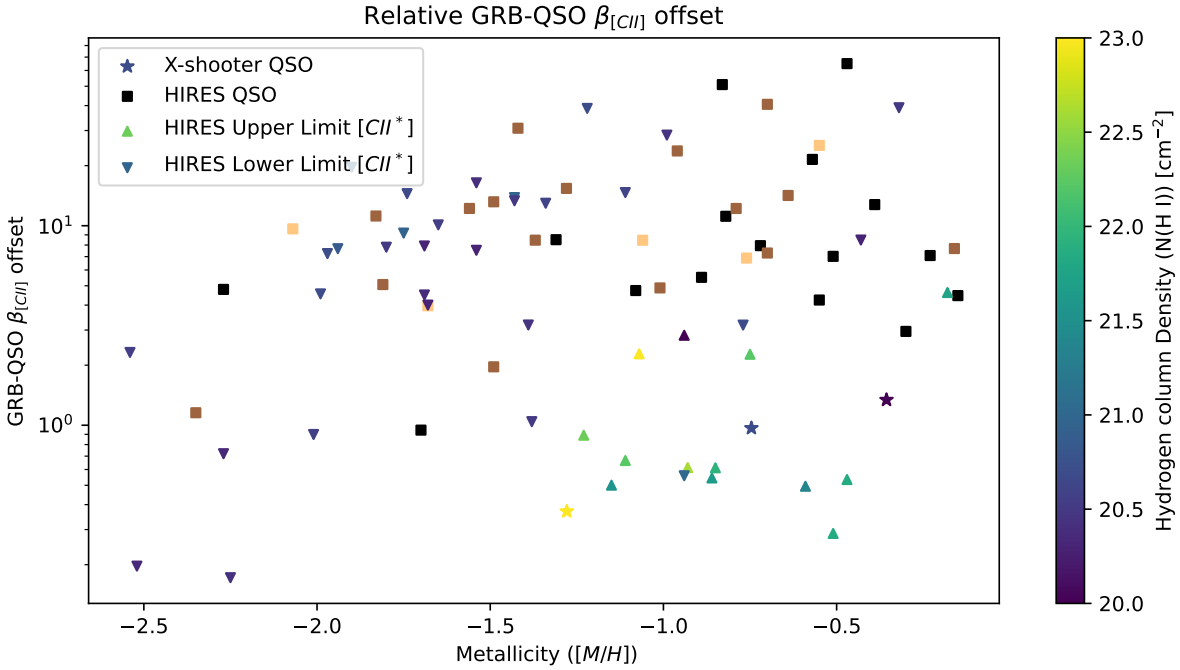

Figure 4.4: The QSO offset of $\beta_{[CII^*]}$ relationship with respect to GRB relation from Heintz et al. (2021)

Statistically QSO sightlines pass at much higher impact parameters compared to GRB which are from the star forming regions (Prochaska et al. 2008). The QSO sightlines usually pass through the extended envelope of H I rather than the star forming gas clouds. Hence they do not trace the star formation gas. The consequence of this is that [C II] cannot be excited by star formation and as suggested by Heintz et al. (2021) shocked gas would be a possible explanation to the lower [C II] emission (Appleton et al. 2013). The result of which is that there is less [C II*] absorption transitions in the sightline. This can be seen in the GRB and QSO relation's Y-intercept of the linear regression. QSO relation shows a 10 times higher $\log \beta_{[\mathrm{C\,II}]}$ as compared to GRB relation which suggests that there is a lower population of stars at [C II] transition at higher impact parameters. The GRB relation is shown to be accurately describing the H I gas mass of nearby galaxies checked using 21 cm transition (Heintz et al. 2021). Thus it can be concluded that using [C II] as a tracer for H I gas mass using QSO sightlines is not feasible.

The slope of the GRB and QSO sightlines are approximately the same and the difference may originate in the statistical variation of the data, and can be predicted to be the same

if further studies are conducted on the QSO and GRB $\beta_{[\mathrm{C\,II}]}$ metallicity relations, the slope would approach each other. Another reason to why the QSO values were higher was the value for Einstein A coefficient used in this report is lower than the value used in (Heintz et al. 2021). As seen in equation 3.3, a lower $A_{[\mathrm{C\,II}]}$ leads to a higher value of $\beta_{[\mathrm{C\,II}]}$. The coefficient used in this study is the latest value released by NIST database (Kramida & Haris 2022). One benefit of using QSO sightlines is the fact that it contains information about star formation efficiently when compared with the GRB relation.

Chapter 5

Conclusion

This study focuses on understanding the feasibility of using [C II*] emission on QSO sightlines to study H I gas mass. The 83 QSO-DLA were selected from two different SDSS surveys. Using HIRES spectroscope in Hawaii and the X-shooter instrument in Chile 80 and 3 QSOs respectively had their spectrum observed. The X-shooter QSOs were further manually fitted for absorption lines using `VoigtFit` while HIRES QSOs were already analysed and column densities were published. By selecting the relevant column densities (H I and [C II*]), the $\beta_{[\mathrm{C\,II}]}$ was determined using equation 3.4. They were plotted against metallicity and normalised for H I column densities. There was a decreasing linear relationship between the two quantities. The QSO relation was found by fitting a linear regression onto the data set of 83 QSO sightlines. The QSO relation was plotted against the linear GRB relation by Heintz et al. (2021). Although the slopes of both the relation's were approximately the same, the QSO relation was shifted up. Two different reasons were stated for why the QSO was higher in value as compared to GRB:

1. The QSO sightline does not pass through star forming regions which enables the increased [C II] absorption due to which lower [C II*] is measured.

2. The Einstein coefficient used in Heintz et al. (2021) was slightly higher than the one used when calibrating [C II] to H I using QSO sightlines.

Thus it can be concluded that using [C II] as a tracer for H I gas mass using QSO sightlines is not feasible and is more valid for GRB sighlines.

Bibliography

Appleton, P. N., Guillard, P., Boulanger, F., et al. 2013, ApJ, 777, 66

Asplund, M., Grevesse, N., Sauval, A. J., & Scott, P. 2009, ARA&A, 47, 481

Burbidge, E. M., Burbidge, G. R., Fowler, W. A., & Hoyle, F. 1957, Rev. Mod. Phys., 29, 547

Carniani, S., Maiolino, R., Smit, R., & Amorín, R. 2018, ApJ, 854, L7

Cia, A. D., Ledoux, C., Mattsson, L., et al. 2016, A&A, 596, A97

Elvis, M. 2000, ApJ, 545, 63

Fernández, X., Gim, H. B., van Gorkom, J. H., et al. 2016, ApJ, 824, L1

Foot, C. J. 2005, Einstein A and B coefficients (Oxford University Press), 11–13

Fox, A. J., Petitjean, P., Ledoux, C., & Srianand, R. 2007, A&A, 465, 171

Fujimoto, S., Ouchi, M., Ferrara, A., et al. 2019, ApJ, 887, 107

Fynbo, J., Leloudas, G., Maund, J., et al. 2011, 413, 2481

Fynbo, J. P. U., Geier, S. J., Christensen, L., et al. 2013, MNRAS, 436, 361

Fynbo, J. P. U., Jakobsson, P., Prochaska, J. X., et al. 2009, ApJS, 185, 526

Ganguly, R., Sembach, K. R., Tripp, T. M., & Savage, B. D. 2005, ApJS, 157, 251

García, T. T. 2006, MNRAS, 369, 2025

Glover, S. C. O. & Clark, P. C. 2012, MNRAS

Graham, A. W. & Driver, S. P. 2005, Publ. Astron. Soc. Aust, 22, 118

Harikane, Y., Ouchi, M., Inoue, A. K., et al. 2020, ApJ, 896, 93

Heintz, K. E., Watson, D., Oesch, P. A., Narayanan, D., & Madden, S. C. 2021, ApJ, 922, 147

Herrera-Camus, R., Förster Schreiber, N., Genzel, R., et al. 2021, A&A, 649, A31

Hjerting, F. 1938, ApJ, 88, 508

Hoppmann, L., Staveley-Smith, L., Freudling, W., et al. 2015, A blind HI Mass Function from the Arecibo Ultra-Deep Survey (AUDS)

Kramida, A. 2010, Atomic Data and Nuclear Data Tables, 96, 586

Kramida, A. & Haris, K. 2022, ApJS, 260, 11

Krogager, J.-K. 2018, VoigtFit: A Python package for Voigt profile fitting

Krogager, J.-K., Møller, P., Fynbo, J. P. U., & Noterdaeme, P. 2017, MNRAS, 469, 2959

Li, W., Amarsi, A. M., Papoulia, A., Ekman, J., & Jönsson, P. 2021, MNRAS, 502, 3780

Magdis, G. E., Daddi, E., Bé thermin, M., et al. 2012, AJ, 760, 6

Mamajek, E. E., Prsa, A., Torres, G., et al. 2015, IAU 2015 Resolution B3 on Recommended Nominal Conversion Constants for Selected Solar and Planetary Properties

Matthee, J., Sobral, D., Boogaard, L. A., et al. 2019, AJ, 881, 124

Nagamine, K., Springel, V., & Hernquist, L. 2004, MNRAS, 348, 421

Neeleman, M., Prochaska, J. X., & Wolfe, A. M. 2015, ApJ, 800, 7

Neeleman, M., Wolfe, A. M., Prochaska, J. X., & Rafelski, M. 2013, ApJ, 769, 54

Olsen, K. P., Burkhart, B., Low, M.-M. M., et al. 2021, ApJ, 922, 88

Papadopoulos, P. P., Thi, W.-F., & Viti, S. 2004, MNRAS, 351, 147

Pineda, J. L., Langer, W. D., & Goldsmith, P. F. 2014, A&A, 570, A121

Planck Collaboration, Aghanim, N., Akrami, Y., et al. 2020, A&A, 641, A6

Prochaska, J. X., Chen, H.-W., Wolfe, A. M., Dessauges-Zavadsky, M., & Bloom, J. S. 2008, ApJ, 672, 59

Ramos Padilla, A. F., Wang, L., Ploeckinger, S., van der Tak, F. F. S., & Trager, S. C. 2021, A&A, 645, A133

Richards, G. T., Fan, X., Schneider, D. P., et al. 2001, AJ, 121, 2308

Robertson, B. E. & Ellis, R. S. 2012, ApJ, 744, 95

Schady, P. 2017, Gamma-ray bursts and their use as cosmic probes

Selsing, J., Malesani, D., Goldoni, P., et al. 2019, A&A, 623, A92

Sersic, J. L. 1968, Atlas de Galaxias Australes

Sparke, L. S. & Gallagher, J. S. 2010, Active galactic nuclei and the early history of galaxies, 2nd edn. (Cambridge Univ. Press), 365–406

Storrie-Lombardi, L. J. & Wolfe, A. M. 2000, ApJ, 543, 552

Tacconi, L. J., Genzel, R., Neri, R., et al. 2010, Nature, 463, 781

Tarantino, E., Bolatto, A. D., Herrera-Camus, R., et al. 2021, ApJ, 915, 92

Tiesinga, E., Mohr, P. J., Newell, D. B., & Taylor, B. N. 2021, Rev. Mod. Phys., 93, 025010

Vernet, J., Dekker, H., D'Odorico, S., et al. 2011, A&A, 536, A105

Wahlgren, G. M. 2010, in EAS Publications Series, Vol. 43, EAS Publications Series, ed. R. Monier, B. Smalley, G. Wahlgren, & P. Stee, 91–114

Wolfe, A. M., Gawiser, E., & Prochaska, J. X. 2005, ARA&A, 43, 861

Wolfe, A. M., Turnshek, D. A., Smith, H. E., & Cohen, R. D. 1986, ApJS, 61, 249

Wolfire, M. G., McKee, C. F., Hollenbach, D., & Tielens, A. G. G. M. 2003, ApJ, 587, 278

Woosley, S. & Bloom, J. 2006, ARA&A, 44, 507

Zanella, A., Daddi, E., Magdis, G., et al. 2018, MNRAS, 481, 1976

Appendix A

Effective Resolution of X-shooter spectrum with respect to the seeing

Table A.1: X-Shooter QSO's resolution

QSO	Seeing [″]	Effective UVB Resolution	Effective VIS Resolution
Q0918+1636	0.69	6400±210	10700±360
Q1313+1414	0.74	6400±220	10700±360
PKS0458-020	1.86	Nominal UVB Resolution	Nominal VIS Resolution

Appendix B

X-Shooter Data Table

Table B.1: Analysed X-shooter Data

QSO	$z_{\rm DLA}$	$\log N({\rm H\,I})$ [cm^{-2}]	[X/H]	X	$\log N([{\rm C\,II}^*])$ [cm^{-2}]	Limit flag
Q1313+1441	1.794	21.270±0.040	-0.746±0.065	Zn	14.892±0.058	
Q0918+1636	2.582	21.067±0.006	-0.356±0.045	Zn	14.956±0.059	
PKS0458-02	2.039	21.946±0.012	-1.279±0.122	Si	15.602±0.139	

Appendix C

HIRES Data Table

Table C.1: Analysed HIRES data

QSO	$z_{\rm DLA}$	$\log N(\mathrm{H\,I})$ [cm^{-2}]	[X/H]	X	$\log N([\mathrm{C\,II^*}])$ [cm^{-2}]	Limit flag
Q1157+014	1.9437	21.70±0.10	-1.23	Si	14.75±0.00	>
Q1215+33	1.9991	20.95±0.06	-1.43	Si	13.18±0.00	<
Q0458-02	2.0395	21.65±0.09	-1.11	Si	14.88±0.00	>
J2340-0053	2.0545	20.35±0.15	-0.55	S	13.72±0.01	
Q2206-19	2.0762	20.43±0.06	-2.25	Si	13.20±0.00	<
Q2359-02	2.0950	20.70±0.10	-0.72	Si	13.69±0.06	
Q0149+33	2.1407	20.50±0.10	-1.43	Si	12.79±0.00	<
Q2348-14	2.2794	20.56±0.07	-2.01	S	13.19±0.00	<
J2036-0553	2.2805	21.20±0.15	-1.81	S	13.41±0.03	
J1435+5359	2.3427	21.05±0.10	-1.42	S	12.88±0.03	
Q2343+125	2.4313	20.34±0.10	-0.47	Si	12.68±0.11	
J1541+3153	2.4435	20.95±0.10	-1.49	Si	13.07±0.09	
Q0836+11	2.4652	20.60±0.10	-1.11	Si	13.13±0.00	<
Q2344+12	2.5379	20.36±0.10	-1.69	Si	12.84±0.00	<
Q0913+072	2.6184	20.35±0.10	-2.52	Si	12.77±0.00	<
Q1759+75	2.6253	20.80±0.10	-0.70	S	13.14±0.03	
J1035+5440	2.6840	20.50±0.20	-0.94	Zn	13.21±0.00	>
PKS1354-17	2.7800	20.30±0.15	-1.31	Si	12.75±0.06	
HS1132+2243	2.7834	21.00±0.07	-1.90	S	12.69±0.00	<
Q1337+11	2.7958	20.95±0.10	-1.75	S	13.11±0.00	<
J1353+5328	2.8349	20.80±0.10	-1.37	S	13.20±0.05	
J1131+6044	2.8757	20.50±0.15	-1.80	O	12.73±0.00	<
J1304+1202	2.9131	20.55±0.15	-1.65	S	12.81±0.00	<
J1304+1202	2.9289	20.30±0.15	-1.54	S	12.77±0.00	<
Q1021+30	2.9489	20.70±0.10	-1.97	S	12.76±0.00	<
J1014+4300	2.9588	20.50±0.10	-0.83	Si	12.63±0.06	
J1410+5111	2.9642	20.85±0.20	-1.94	Si	13.01±0.00	<

HS0741+4741	3.0174	20.40±0.10	-1.54	S	12.51±0.00	<
J1240+1455	3.0241	20.45±0.10	-1.39	S	13.31±0.00	<
Q0347-38	3.0247	20.60±0.10	-1.08	Si	13.47±0.03	
Q0336-01	3.0620	21.20±0.10	-1.49	S	14.00±0.01	
J1200+4015	3.2200	20.85±0.10	-0.64	S	13.68±0.02	
Q0930+28	3.2352	20.30±0.10	-1.69	O	12.57±0.00	<
J0900+4215	3.2458	20.30±0.10	-0.82	S	13.07±0.03	
J0929+2825	3.2627	21.10±0.10	-1.56	S	13.19±0.02	
J2315+1456	3.2732	20.30±0.15	-1.68	S	12.88±0.00	<
BR0019-15	3.4388	20.92±0.10	-1.01	Si	13.84±0.01	
J0814+5029	3.7075	21.35±0.15	-2.07	S	13.09±0.04	
BRI1346-03	3.7358	20.72±0.10	-2.27	Si	12.55±0.12	
PSS0209+05	3.8635	20.55±0.10	-2.54	Si	12.51±0.00	<
J1051+3107	4.1392	20.70±0.20	-1.99	S	13.01±0.00	<
PSS1443+27	4.2241	21.00±0.10	-0.94	Fe	14.68±0.00	<
J0817+1351	4.2584	21.30±0.15	-1.15	S	14.40±0.00	>
J1100+1122	4.3947	21.74±0.10	-1.68	Fe	14.15±0.02	
J1607+1604	4.4741	20.30±0.15	-1.70	Si	13.10±0.09	
J1200+4618	4.4765	20.50±0.15	-1.38	Fe	13.73±0.00	<
J1202+3235	4.7955	21.10±0.15	-2.35	Fe	13.29±0.02	
J1051+3545	4.8206	20.35±0.10	-2.27	Si	12.83±0.00	<
J1056+1208	1.6093	21.45±0.15	-0.47	Si	15.65±0.00	>
J0044+0018	1.7250	20.35±0.10	-0.23	S	13.81±0.03	
J0927+1543	1.7311	21.35±0.15	-0.86	Si	15.22±0.00	>
J0008-0958	1.7675	20.85±0.15	-0.16	S	14.34±0.01	
J1249-0233	1.7808	21.45±0.15	-1.06	S	14.12±0.01	
J0233+0103	1.7850	20.60±0.15	-1.34	Si	13.03±0.00	<
J1454+0941	1.7884	20.50±0.15	-0.39	S	13.59±0.06	
J1313+1441	1.7947	21.20±0.15	-0.59	Si	15.26±0.00	>
J1310+5424	1.8005	21.45±0.15	-0.51	Si	15.43±0.00	>
J1106+1044	1.8185	20.50±0.15	-0.32	S	13.36±0.00	<
J1142+0701	1.8407	21.50±0.15	-0.85	Si	14.83±0.00	>
J0815+1037	1.8462	20.30±0.15	-0.43	Si	13.69±0.00	<
J1335+0824	1.8560	20.65±0.15	-0.51	S	13.87±0.05	
J1024+0600	1.8950	20.60±0.15	-0.30	S	14.31±0.01	
J1524+1030	1.9409	21.65±0.15	-0.75	Zn	14.76±0.00	>
J1042+0628	1.9429	20.70±0.15	-0.77	S	14.15±0.00	<
J1417+4132	1.9508	21.85±0.15	-0.93	Zn	15.11±0.00	>
J1552+4910	1.9599	21.15±0.15	-0.96	S	13.49±0.03	
Q1755+578	1.9692	21.40±0.15	-0.18	Zn	14.77±0.00	>
J1305+0924	2.0184	20.40±0.15	-0.15	S	14.10±0.04	
J1509+1113	2.0283	21.30±0.15	-0.76	S	14.31±0.03	
J1135-0010	2.2068	22.05±0.10	-1.07	Si	15.00±0.00	>

J1211+0422	2.3765	20.70±0.10	-1.22	S	12.73±0.00	<
J2241+1225	2.4179	21.15±0.10	-1.28	Fe	13.39±0.09	
J0211+1241	2.5951	20.60±0.15	-0.57	Si	13.32±0.03	
J0812+3208	2.6263	21.35±0.10	-0.55	O	14.02±0.01	
J1558-0031	2.7026	20.67±0.05	-1.74	S	12.60±0.00	<
FJ2334-09	3.0569	20.45±0.10	-0.99	Si	12.81±0.00	<
J2100-0641	3.0924	21.05±0.15	-0.70	S	14.09±0.01	
J1155+0530	3.3260	21.05±0.10	-0.79	S	13.81±0.02	
J0825+3544	3.6567	21.25±0.10	-1.83	Si	13.14±0.05	
J0909+3303	3.6581	20.55±0.10	-0.89	S	13.53±0.08	

Appendix D

X-Shooter Spectrum

D.1 Q0918+1636

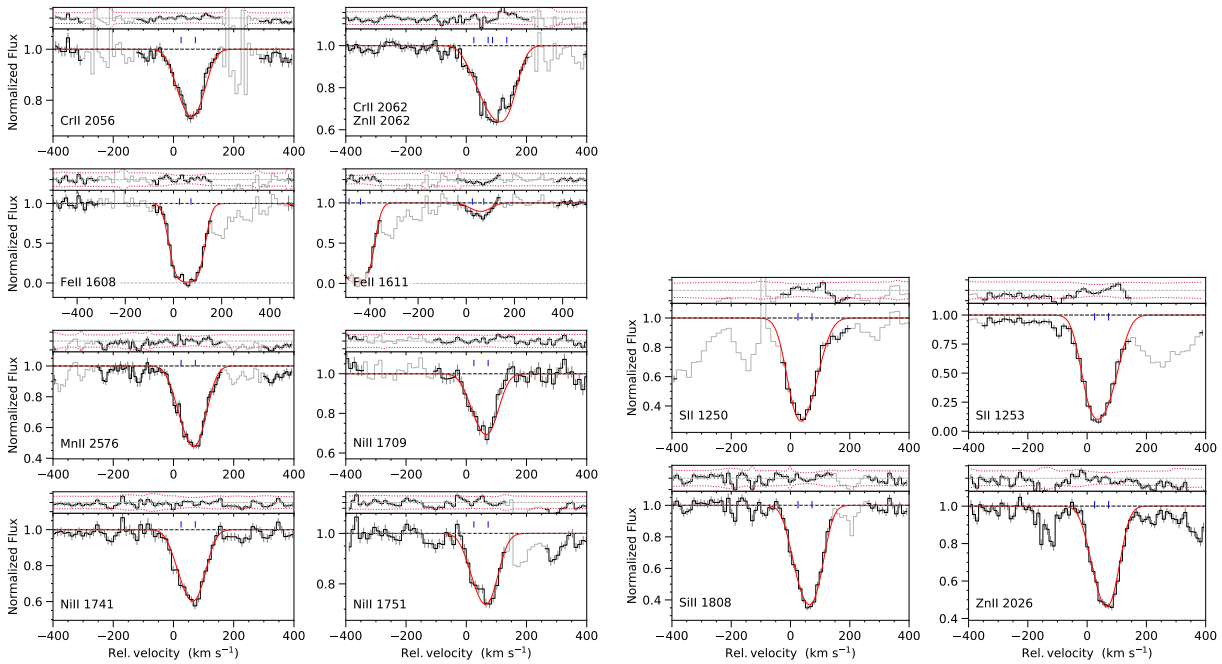

Figure D.1: Metal absorption lines of Q0918+1636

D.2 Q1313+1441

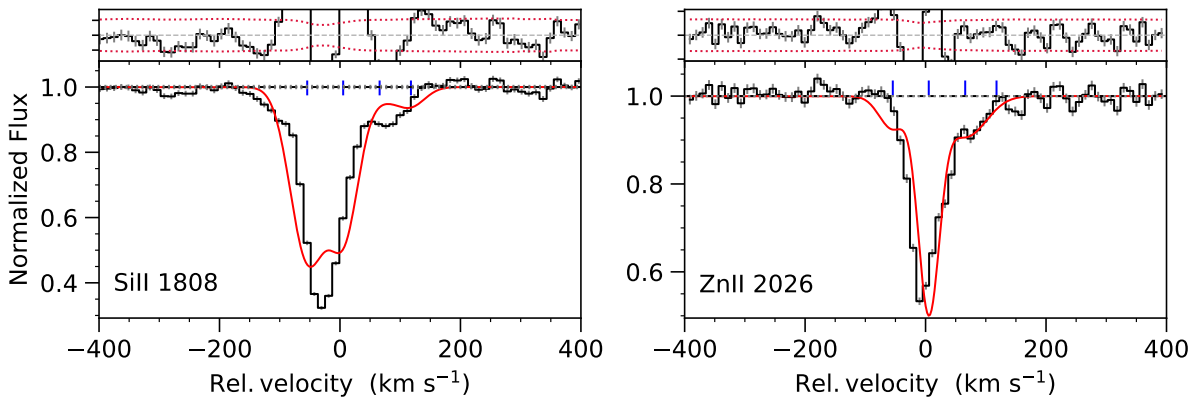

Figure D.2: Metal absorption lines of Q1313+1441

D.3 PSK0458-020

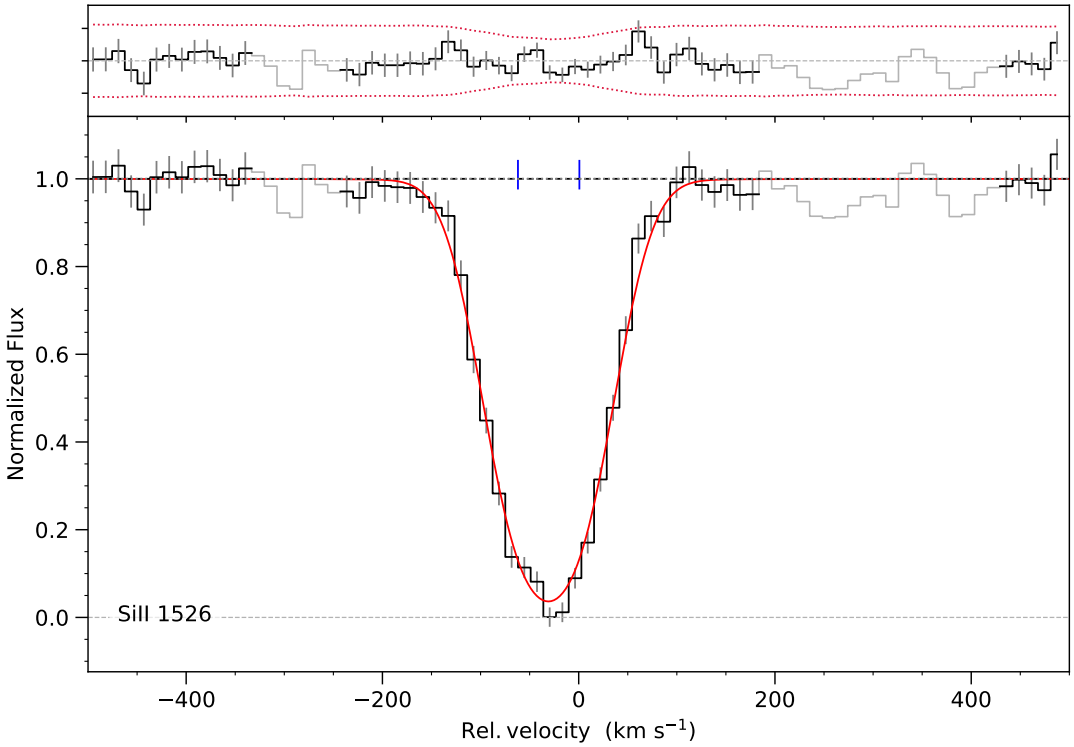

Figure D.3: Si II absorption line of PSK0458-020

Appendix E

$\beta_{[\mathrm{C\,II}]}$ results

Table E.1: Results table containing the derived $\beta_{[\mathrm{C\,II}]}$ for each QSO-DLA

QSO	z_{DLA}	$\log \beta_{[\mathrm{C\,II}]}$
Q1313+1441	1.7940	2.423±0.095
Q0918+1636	2.5820	2.159±0.084
PKS0458-02	2.0390	2.392±0.197
Q1157+014	1.9437	2.998±0.141
Q1215+33	1.9991	3.818±0.085
Q0458-02	2.0395	2.818±0.127
J2340-0053	2.0545	2.678±0.213
Q2206-19	2.0762	3.278±0.085
Q2359-02	2.0950	3.058±0.165
Q0149+33	2.1407	3.758±0.141
Q2348-14	2.2794	3.418±0.099
J2036-0553	2.2805	3.838±0.216
J1435+5359	2.3427	4.218±0.148
Q2343+125	2.4313	3.708±0.210
J1541+3153	2.4435	3.928±0.190
Q0836+11	2.4652	3.518±0.141
Q2344+12	2.5379	3.568±0.141
Q0913+072	2.6184	3.628±0.141
Q1759+75	2.6253	3.708±0.148
J1035+5440	2.6840	3.338±0.283
PKS1354-17	2.7800	3.598±0.228
HS1132+2243	2.7834	4.358±0.099
Q1337+11	2.7958	3.888±0.141
J1353+5328	2.8349	3.648±0.158
J1131+6044	2.8757	3.818±0.212
J1304+1202	2.9131	3.788±0.212

J1304+1202	2.9289	3.578±0.212
Q1021+30	2.9489	3.988±0.141
J1014+4300	2.9588	3.918±0.165
J1410+5111	2.9642	3.888±0.283
HS0741+4741	3.0174	3.938±0.141
J1240+1455	3.0241	3.188±0.141
Q0347-38	3.0247	3.178±0.148
Q0336-01	3.0620	3.248±0.142
J1200+4015	3.2200	3.218±0.144
Q0930+28	3.2352	3.778±0.141
J0900+4215	3.2458	3.278±0.148
J0929+2825	3.2627	3.958±0.144
J2315+1456	3.2732	3.468±0.212
BR0019-15	3.4388	3.128±0.142
J0814+5029	3.7075	4.308±0.220
BRI1346-03	3.7358	4.218±0.221
PSS0209+05	3.8635	4.088±0.141
J1051+3107	4.1392	3.738±0.283
PSS1443+27	4.2241	2.368±0.141
J0817+1351	4.2584	2.948±0.212
J1100+1122	4.3947	3.638±0.144
J1607+1604	4.4741	3.248±0.247
J1200+4618	4.4765	2.818±0.212
J1202+3235	4.7955	3.858±0.214
J1051+3545	4.8206	3.568±0.141
J1056+1208	1.6093	1.848±0.212
J0044+0018	1.7250	2.588±0.148
J0927+1543	1.7311	2.178±0.212
J0008-0958	1.7675	2.558±0.213
J1249-0233	1.7808	3.378±0.213
J0233+0103	1.7850	3.618±0.212
J1454+0941	1.7884	2.958±0.228
J1313+1441	1.7947	1.988±0.212
J1310+5424	1.8005	2.068±0.212
J1106+1044	1.8185	3.188±0.212
J1142+0701	1.8407	2.718±0.212
J0815+1037	1.8462	2.658±0.212
J1335+0824	1.8560	2.828±0.224
J1024+0600	1.8950	2.338±0.213
J1524+1030	1.9409	2.938±0.212
J1042+0628	1.9429	2.598±0.212
J1417+4132	1.9508	2.788±0.212
J1552+4910	1.9599	3.708±0.216

Q1755+578	1.9692	2.678±0.212
J1305+0924	2.0184	2.348±0.220
J1509+1113	2.0283	3.038±0.216
J1135-0010	2.2068	3.098±0.141
J1211+0422	2.3765	4.018±0.141
J2241+1225	2.4179	3.808±0.190
J0211+1241	2.5951	3.328±0.216
J0812+3208	2.6263	3.378±0.142
J1558-0031	2.7026	4.118±0.071
FJ2334-09	3.0569	3.688±0.141
J2100-0641	3.0924	3.008±0.213
J1155+0530	3.3260	3.288±0.144
J0825+3544	3.6567	4.158±0.158
J0909+3303	3.6581	3.068±0.181